Article

The Phase Composition and Microstructure of Al$_x$CoCrFeNiTi Alloys for the Development of High-Entropy Alloy Systems

Thomas Lindner *, Martin Löbel, Thomas Mehner, Dagmar Dietrich and Thomas Lampke

Materials and Surface Engineering Group, Institute of Materials Science and Engineering,
Technische Universität Chemnitz, D-09125 Chemnitz, Germany; martin.loebel@mb.tu-chemnitz.de (M.L.);
thomas.mehner@mb.tu-chemnitz.de (T.M.); dagmar.dietrich@mb.tu-chemnitz.de (D.D.);
thomas.lampke@mb.tu-chemnitz.de (T.L.)
* Correspondence: th.lindner@mb.tu-chemnitz.de; Tel.: +49-371-531-38287

Abstract: Alloying aluminum offers the possibility of creating low-density high-entropy alloys (HEAs). Several studies that focus on the system AlCoCrFeNiTi differ in their phase determination. The effect of aluminum on the phase composition and microstructure of the compositionally complex alloy (CCA) system Al$_x$CoCrFeNiTi was studied with variation in aluminum content (molar ratios x = 0.2, 0.8, and 1.5). The chemical composition and elemental segregation was measured for the different domains in the microstructure. The crystal structure was determined using X-ray diffraction (XRD) analysis. To identify the spatial distribution of the phases found with XRD, phase mapping with associated orientation distribution was performed using electron backscatter diffraction. This made it possible to correlate the chemical and structural conditions of the phases. The phase formation strongly depends on the aluminum content. Two different body-centered cubic (bcc) phases were found. Texture analysis proved the presence of a face-centered cubic (fcc) phase for all aluminum amounts. The hard η-(Ni, Co)$_3$Ti phase in the x = 0.2 alloy was detected via metallographic investigation and confirmed via electron backscatter diffraction. Additionally, a centered cluster (cc) with the A12 structure type was detected in the x = 0.2 and 0.8 alloys. The correlation of structural and chemical properties as well as microstructure formation contribute to a better understanding of the alloying effects concerning the aluminum content in CCAs. Especially in the context of current developments in lightweight high-entropy alloys (HEAs), the presented results provide an approach to the development of new alloy systems.

Keywords: HEA; high-entropy alloy; CCA; compositionally complex alloy; phase composition; microstructure

1. Introduction

Previous material research and the development of alloy systems have been focused on compositions with one main element providing the primary characteristics. Until now, the improvement of these properties has mainly been achieved by alloying small amounts of other elements. A relatively new approach is the study of multicomponent alloy systems with nearly equimolar amounts of elements. Since the first publications in 2004, research on HEA systems, also designated as CCA, obtains an increasing scientific interest [1,2]. HEA refers to single-phase alloys, while CCA indicates at least two phases in the microstructure [3]. The fact that a minimum number of five different elements can build a simple cubic crystal structure with promising material properties is the main cause of the great number of development efforts [4]. The possibilities of alloy variations are almost unlimited.

Cantor et al. were the first to develop a single fcc phase alloy system consisting of different transition metals [1]. Further mentioned phases include bcc, hexagonal closed packed (hcp), and mixed solid solution structures, as well as different intermetallic phases. Generally, element ratios of 5–35 atom %, but not over 50 atom %, are characteristic of the composition of HEAs [4]. The AlCoCrCuFeNi system and the copper-free AlCoCrFeNi system are the most studied HEA systems [5–7]. Based on these alloy systems, different modifications have been investigated [8–11]. Hume-Rothery et al. [12] pointed out a tendency for a definite crystal structure at a particular electron concentration. Guo et al. [13] used the valence electron concentration (VEC) for the prediction of a preferred crystal structure in HEA where VEC < 6.87 (bcc), VEC = 6.87–8.0 (bcc+fcc), and VEC > 8.0 (fcc). Zhu et al. [14] shifted the bcc+fcc region to VEC = 7.3–8.1. Based on the molar ratio, the VEC is calculated according to Equation (1), with the atomic concentration c_i and the valence electron concentration $(VEC)_i$ for alloying element *i*:

$$VEC = \sum_{i=1}^{n} c_i (VEC)_i \tag{1}$$

The investigation of the influence of different alloying elements on phase composition is another area of interest. For example, a titanium addition has a large strengthening effect and usually favors the formation of intermetallic phases due to its large negative enthalpy while mixing with other elements in the composition. A variation in aluminum content has a significant effect on the microstructure and physical properties [15]. The initial approach that HEAs form a simple solid solution in a bcc or fcc structure proved to be an exception. The majority of studied HEAs seem to build a complex structure sensitive to changes in chemical composition [16]. Furthermore, a clear identification of the different phases with characteristic lattice parameters and chemical compositions provides the basis for sophisticated alloy development. Wu et al. [17] found a phase in the $CoCrCu_xFeMoNi$ system with the space group of $I\bar{4}3m$, which they attributed to a simple bcc structure with the lattice parameter of $a = 8.90$ Å. Feng et al. [18] also found this phase in the aluminum rich $Al_{3-4}CrFeMnTi_{0.25}$ system and identified it as an Al_8Cr_5 type. It seems that Zhang et al. [15] detected this phase in the $Al_{0.5-1.0}CoCrFeNiTi$ system as well but did not assign it as the $I\bar{4}3m$ space group; they assumed intermetallic phases of $CoTi_2$ and FeTi. Soare et al. [19] found that the equimolar AlCoCrFeNiTi leads to the formation of two complex phases with $D0_3$ and the A12 structure type. The A12 structure is a centered cluster (cc) phase that pertains to the group of topologically close-packed structures (Frank–Kasper phases) characterized by brittleness and low formability. Chuang et al. [20] found for $Al_{0.2}Co_{1.5}CrFeNi_{1.5}Ti_{0.5}$ the presence of a hard η-(Ni, Co)$_3$Ti phase. Lee et al. [21] studied $Al_{0.5}CoCrNiTi_{0.5}$ and found similar characteristic peaks for the A12 structure type, which he assigned as $D8_b$. His aging experiments in the temperature range of 773 to 1473 K show that the cc phase was dissolved after 24 h at 1473 K. Overall, the phase detection and attribution to chemical domains in the HEA systems are current problems that need further research. A recent comprehensive review on high-entropy alloys was provided by Gao et al. [22].

This study focuses on the alloy system $Al_xCoCrFeNiTi$ with various aluminum content values. Phase formation and microstructural evolution depending on the change in chemical composition are studied. The different phase types are clearly identified and lattice parameters are assigned. This will contribute to a better understanding of the effects of aluminum alloying in HEAs. The criteria of phase prediction are reviewed regarding their correctness.

2. Materials and Methods

High-purity elements were mixed in the intended molar ratio in order to produce three different alloys in the $Al_xCoCrFeNiTi$ system. Granulates with a chemical purity of over 99.9% were used. Alloy samples with a mass of 10 g and target compositions according to Table 1 were arc-melted with a cooling rate of <50 K/s.

Table 1. Target composition of the three alloys.

Element	Al	Co	Cr	Fe	Ni	Ti
atom %	3.9	19.2	19.2	19.2	19.2	19.2
wt %	1.9	21.1	18.7	20.0	21.1	17.2
x	0.2	1	1	1	1	1
atom %	13.8	17.2	17.2	17.2	17.2	17.2
wt %	7.3	20.0	17.7	18.9	19.9	16.2
x	0.8	1	1	1	1	1
atom %	23.1	15.4	15.4	15.4	15.4	15.4
wt %	12.9	18.8	16.6	17.8	18.7	15.3
x	1.5	1	1	1	1	1

The furnace was flooded with argon after reaching a pressure of 2×10^{-4} mbar. After the arc was ignited with a tungsten electrode, the high purity elements were cast into a copper crucible with a diameter of about 20 mm. The arc-furnace parameters are shown in Table 2. The samples were remolded three times in order to achieve a homogeneous element distribution.

Table 2. Arc-furnace parameters.

Mean Quantity (g)	Droplet Size (mm)	Vacuum Pressure (mbar)	Argon Pressure (bar)	Gas Purity (%)	Current (A)
10	20	2×10^{-4}	1.1	99.9999	250

The heat flow during solidification was recorded in a temperature range from 1800 K to room temperature by differential scanning calorimetry (DSC) STA 409 C (Netzsch, Selb, Germany) with a cooling rate of 20 K/min. Metallographic cross sections of the cast samples were prepared according to standard metallographic procedures by hot mounting in conductive resin, grinding, and polishing. The microstructure and the averaged as well as the phase selective chemical composition were investigated by backscattered electron imaging (BSD) in conjunction with energy-dispersive X-ray spectroscopy (EDS) measurement in a scanning electron microscope LEO 1455VP (Zeiss, Jena, Germany) equipped with an EDS spectrometer (GENESIS, EDAX, Mahwah, NJ, USA). The crystallographic studies were performed on all samples by X-ray diffraction (XRD) using a D8 DISCOVER diffractometer from Bruker AXS (Billerica, MA, USA). Co Kα radiation was used with a tube voltage of 40 kV, a tube current of 40 mA, polycap optics for beam shaping, a 1 mm pinhole collimator, and a 1D Lynxeye XE detector. The diffraction diagrams were measured in the diffraction angle (2θ) range from 20° to 129° with a step size of 0.01°, and 1.5 s/step, which corresponds to 288 s/step due to the use of the 1D detector. The powder diffraction file (PDF) database 2014 was applied for phase identification. Texture measurements were performed utilizing a D5000 diffractometer (Bruker AXS, Billerica, MA, USA) with Co Kα radiation (tube parameters: 35 kV, 30 mA) and a 1 mm pinhole collimator using a scintillation counter. The diffraction angle was set to 30.5° with tilt angles of 0°–80° and step sizes of 5° for both tilt and rotation angles with 2 s/step. For phase localization, the samples were studied by electron backscatter diffraction (EBSD) using a field emission scanning electron microscope (Zeiss NEON 40EsB, Zeiss, Jena, Germany) equipped with an EBSD system (OIM 5.2, EDAX TSL, Mahwah, NJ, USA) operated at 15 kV in the high current mode with a 60 μm aperture. The step size was 200 nm in a field of 50 μm × 50 μm. The elemental composition was recorded by EDS data collection simultaneously with the EBSD data acquisition. The EBSD data were subjected to a slight cleanup procedure comprising neighbor confidence index (CI) correlation, grain CI standardization with a minimum confidence index of 0.1, and grain dilatation with one iteration step.

3. Results and Discussion

3.1. Chemical Composition of the Cast Samples

The EDS measurements confirm the intended mean chemical composition. Certain deviations can be found in the molar ratio of titanium (Table 3). Aluminum shows good matching, with x = 0.16, 0.83, and 1.47.

Table 3. Average chemical compositions of the three sets of samples measured by EDS.

Element	Al	Co	Cr	Fe	Ni	Ti	VEC
atom %	3.0	19.4	19.9	20.0	20.0	17.7	
wt %	1.5	21.2	19.2	20.7	21.7	15.7	7.3
x	0.16	1.0	1.0	1.0	1.0	0.9	
atom %	14.3	17.4	17.3	17.0	17.9	16.1	
wt %	7.6	20.2	17.7	18.7	20.7	15.2	6.8
x	0.83	1.0	1.0	1.0	1.1	0.9	
atom %	22.7	16.2	15.1	15.4	16.7	13.8	
wt %	12.6	19.7	162	17.7	20.2	13.7	6.5
x	1.47	1.1	1.0	1.0	1.1	0.9	

The VEC was been repeatedly mentioned to be an effective criterion for predicting phase constitution in HEA/CCA. The calculated valence electron concentration according to the chemical composition summarized in Table 3 is 7.3 for x = 0.2, 6.8 for x = 0.8, and 6.5 for x = 1.5. In accordance with previous studies for both x = 0.8 and 1.5, a bcc structure can be predicted, while x = 0.2 fulfills the criterion given by Guo et al. for a mixed bcc+fcc structure [13] and the criterion given by Zhu et al. for a bcc structure [14].

3.2. Melting Behavior of the Cast Samples

The cooling curves of heat flow for the different alloys in the temperature range from 800 to 1800 K verify the formation of a high temperature phase with an increasing aluminum content value (Figure 1).
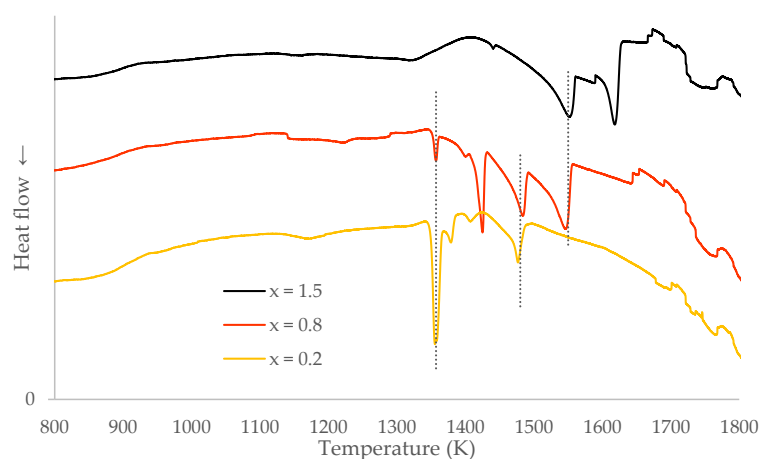

Figure 1. DSC cooling curves of as-cast Al$_x$CoCrFeNiTi alloy.

In the alloy system where x = 1.5, the first exothermic reaction with nucleation of the dendrites of the primary phase takes place at 1620 K. The second and last greater peak in the heat flow can be found at 1550 K for x = 1.5. This corresponds to the first solidification of the x = 0.8 alloy. Lowering the aluminum molar ratio to x = 0.2, the first solidification takes place at 1480 K corresponding with the

second peak of $x = 0.8$. The last exothermic peaks of the $x = 0.2$ and 0.8 alloys are at 1360 K. In case of $x = 0.2$, it is a large peak with a small melting temperature range, indicating a eutectic reaction. The different peaks roughly indicate the number of formed phases, but solid state transformations or formation of precipitations can additionally occur.

3.3. Microstructure of the Cast Samples

The BSD images (Figure 2) confirm a heterogeneous microstructure of the different alloys. The material contrast indicates different phases by different gray levels.

Figure 2. BSD images of the cast Al$_x$CoCrFeNiTi alloy with $x =$ (**a**) 0.2, (**b**) 0.8, and (**c**) 1.5 in overall view (**left**) and in detail (**right**) with phase declaration (PP: primary phase; IP: interdendritic phase; SP: secondary phase; CW: cell wall; IC: intermetallic compound).

With a low aluminum concentration, the contrast between the transition elements is relatively low. Adding more aluminum leads to a higher contrast due to its lower electron backscattering coefficient. Therefore, an aluminum-rich phase appears darker. Small amounts of black particles are visible in all cross-section images. Apart from pores and breakouts formed during preparation, these are intermetallic compound (IC) phases, which are either titanium- or aluminum-rich. As seen in Figure 2b,c, an increasing aluminum content directly influences the primary nucleation. A dendritic structure is formed around the IC particles. This primary phase recorded for $x = 0.8$ and 1.5 causes the DSC peaks at higher temperatures with increasing aluminum amounts. The large grains of the dendritic arms are a result of a broad melting range. Around this high temperature phase, an interdendritic phase nucleates. Only a small amount of this phase nucleates primary around the IC particles for $x = 0.2$. In the $x = 0.2$ and 0.8 systems, the parts around the primary structures solidify in an alternating mixture of secondary phase and cell wall. For $x = 1.5$, only a small amount solidifies as a remainder. Additionally, in the $x = 0.2$ system and to a lower extent in the $x = 0.8$ system, bright needles can be noticed in between the cell walls.

The elemental composition of the different phases was measured by EDS. The atomic ratio was calculated, and the results are shown in Table 4. The chemical composition of the different phases differs significantly from the average molar ratio. The characteristically high chromium and iron content values of the primary phase in the $x = 0.2$ alloy are similar to the interdendritic phase in the $x = 0.8$ and 1.5 alloys. The dendrites of the primary phase for $x = 0.8$ and 1.5 show an elevated aluminum content value. The dendrites of the secondary phase of the $x = 0.2$ alloy contain the lowest concentration of aluminum and correlate well with the composition of the secondary dendrites for $x = 0.8$ and the cell wall of $x = 1.5$. Similarly, the chemical compositions of the cell walls in $x = 0.2$ and $x = 0.8$ alloys match.

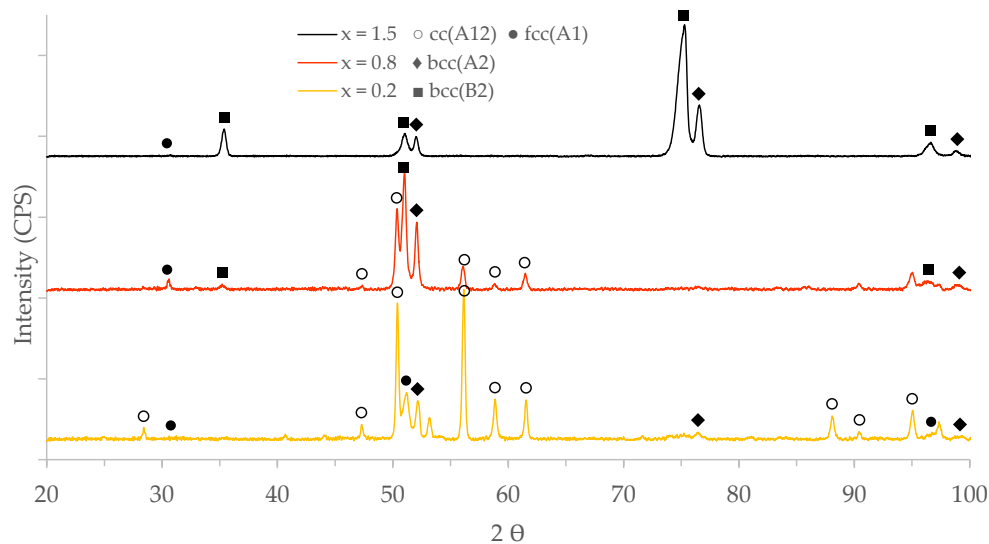**Table 4.** Chemical composition of the phases in atom % measured by EDS.

	Phase	Structure	Al	Co	Cr	Fe	Ni	Ti	Local VEC
	IC		6.7	8.1	13.8	9.5	5.7	56.2	5.34
	primary phase	bcc (A2)	5.2	14.9	38.7	23.6	11.9	5.8	7.12
$x = 0.2$	secondary phase	fcc (A1)	2.1	20.5	23.5	22.4	15.7	15.8	7.31
	cell wall	cc (A12)	8.6	21.1	8.9	12.9	26.2	22.4	7.23
	IC (η-phase)		2.2	19.2	11.1	16.5	30.9	20.0	7.68
	IC		68.3	7.7	2.5	3.6	7.8	10.1	4.37
	primary phase	bcc (B2)	25.8	20.6	4.3	7.5	21.9	20.0	6.47
$x = 0.8$	interdendritic phase	bcc (A2)	4.5	14.5	36.7	27.8	9.7	6.8	7.11
	secondary phase	fcc (A1)	2.6	18.0	24.7	27.4	12.5	14.8	7.22
	cell wall	cc (A12)	9.9	19.2	8.8	15.4	25.9	20.9	7.20
	IC		70.5	4.8	7.6	6.0	4.4	6.7	4.20
$x = 1.5$	primary phase	bcc (B2)	31.1	19.7	4.9	8.4	19.8	16.1	6.30
	interdendritic phase	bcc (A2)	9.6	11.1	36.6	28.5	7.5	6.6	6.78
	cell wall	fcc (A1)	3.6	14.3	22.3	31.0	13.5	15.2	7.18

3.4. Phase Determination

According to Figure 2, a multiphase character can be observed for all alloys, which is proven by the results of XRD measurements shown in Figure 3. For the different alloys, the lattice parameters of similar phases are almost identical. The major crystallographic information is summarized in Table 5.

Table 5. List of phases detected by X-ray diffraction (XRD) measurements.

Struktur-Bericht	Lattice	Structure Type	Pearson Symbol	Space Group	Lattice Parameter (Å)	Detected for *x*
A1	fcc	Cu	cF4	$Fm\bar{3}m$ (225)	a = 5.88	0.2, 0.8, 1.5
A2	bcc	W	cI2	$Im\bar{3}m$ (229)	a = 2.88	0.2, 0.8, 1.5
B2	bcc	CsCl	cP2	$Pm\bar{3}m$ (221)	a = 2.94	0.8, 1.5
A12	centered cluster (cc)	α-Mn	cI58	$I\bar{4}3m$ (217)	a = 8.91	0.2, 0.8

Figure 3. XRD diffraction diagrams of the cast Al$_x$CoCrFeNiTi alloy for *x* = 0.2, 0.8, and 1.5.

A correlation in phase presence can be found between *x* = 0.2 and 0.8 alloys. The low aluminum content promotes the presence of the cc (A12) already mentioned by Soare et al. [19]. With increasing aluminum content, the peak intensity decreases over *x* = 0.8 to absence for *x* = 1.5. The η-phase with space group $P6_3/mmc$ (194) and hcp (D0$_{24}$) structure could not be clearly detected by XRD analysis similarly as mentioned by Chuang et al. [20]. The characteristically high concentrations of nickel, cobalt, and titanium in the needle-shaped IC η-phase were evidenced in the alloys with low aluminum content (Table 4). The peak for *x* = 0.2 at 53.45° could not be assigned. For all three samples, the bcc (A2) type was detected, while the *x* = 0.8 and 1.5 systems also show a chemically ordered bcc (B2) structure. Whereas there is no evidence for textures of both bcc phases (A2, B2) in *x* = 0.2 and *x* = 0.8 compositions, especially for *x* = 1.5, a strong {200} texture was found ({200} peak at angles around 75°). This can be explained by the irradiated area of the XRD measurement (Ø 1.2 mm) in combination with highly local microstructural information and preferred solidification direction. For *x* = 0.8, a peak at an angle of 30.6° characteristic for an fcc (A1) phase was detected. Only this peak clearly differs from the characteristic peaks of bcc (B2), since additional fcc peaks overlap with bcc (B2) peaks. This is in contrast to Soare et al. [19] who assigned a peak at 26.2° (Cu Kα radiation), corresponding the peak at 30.6° (Co Kα radiation) to the complex cubic structure D0$_3$. Nevertheless, a comparison to the referenced PDF 03-065-4682 indicates an fcc (A1) structure.

To verify the existence of the fcc (A1) structure, a texture measurement at the angle of 30.5° using Co Kα radiation was performed. The recorded pole figures shown in Figure 4 clearly indicate the presence of that peak for all samples by tilting the sample, although it did not appear in the measurements shown in Figure 3 because the corresponding lattice planes were not parallel to the sample surface. These analyses confirm that an fcc (A1) structure is present in all samples. This contrasts the prediction criteria of Guo et al. [13] and Zhu et al. [14] for *x* = 1.5. Table 4 shows large variations in chemical composition that affects the local VEC. A general prediction criterion does not appear to be tenable for overall HEA/CCA alloy compositions.
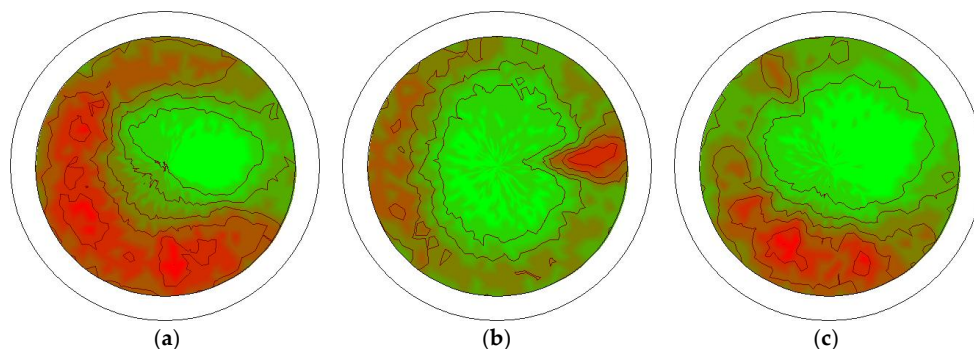
Figure 4. XRD pole figures (in stereographic projection) at 2θ = 30.5° of the {111} lattice planes of the fcc (A1) structure. (**a**) $Al_{0.2}CoCrFeNiTi$; (**b**) $Al_{0.8}CoCrFeNiTi$; (**c**) $Al_{1.5}CoCrFeNiTi$.

3.5. Phase Assignment

Figures 2 and 3 show that increasing aluminum content values is accompanied by a significant change in microstructure. For $x = 0.2$, a fine structure with equal amounts of dendrites and cell walls can be found. In $x = 1.5$, the microstructural changes show large amounts of dendrites of a primary phase surrounded by interdendritic parts, surrounded by cell walls that solidify as a remainder. All phase components, which can be found in the alloys with low and high aluminum content values, are present in the $x = 0.8$ alloy system.

Figure 5 shows the maps of phases and orientations distribution between primary nucleated dendrites in the bcc (A2) structure in the $x = 0.2$ system. The secondary phase shows an fcc (A1) structure and similar orientation. During the formation of the cell walls with the cc (A12) structure, the depletion of aluminum causes the precipitation of the η-phase between two solidification fronts. Consequently, a fine-grained microstructure, which is characterized by multiple orientations, forms.
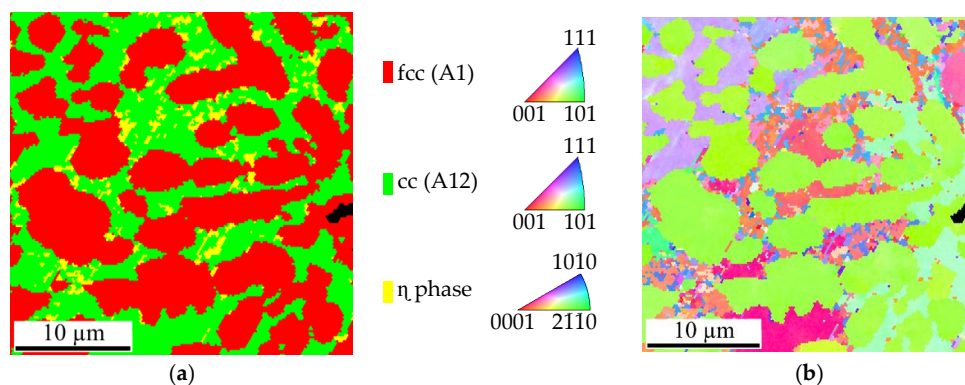

Figure 5. $Al_{0.2}CoCrFeNiTi$ (**a**) phase map and (**b**) orientation distribution, color-coded according to the unit triangle of the inverse pole figure (IPF).

Figure 6 shows a map comprising all revealed phases (except for the tiny and thus hardly discernable η-phase) and the corresponding orientation distribution map of the $x = 0.8$ alloy calculated from EBSD Kikuchi patterns. Similar orientations in the dendrites of the primary phase are evidenced. The surrounding interdendritic phase with high chromium and iron content values shows good orientation matching.
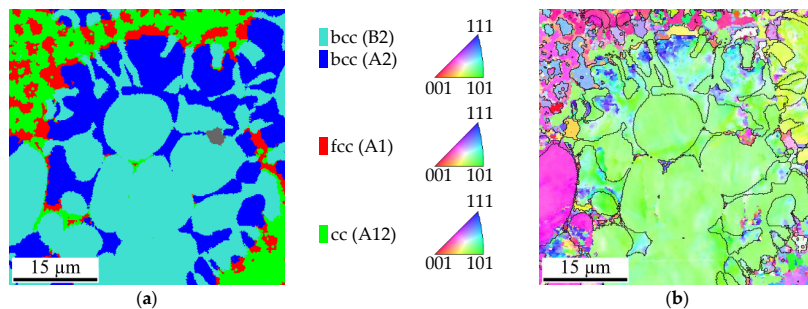
Figure 6. $Al_{0.8}CoCrFeNiTi$ (**a**) phase map and (**b**) orientation distribution, color-coded according to the unit triangle of the (IPF).

The dendrites, which primarily nucleate in the $x = 0.8$ and 1.5 alloys, have the highest aluminum content and a lower concentration of chromium and iron, and are associated with a local VEC of 6.47 or 6.30, respectively, have to be assigned to the bcc (B2) phase. The phase, which is the primary phase in $x = 0.2$ systems and the interdendritic phase in $x = 0.8$ and 1.5 systems, has lower aluminum content, but higher chromium and iron content. This phase, with a local VEC of 7.12 for $x = 0.2$, 7.11 for $x = 0.8$, and 6.78 for $x = 1.5$, respectively, can be identified as a bcc (A2) structure. The local depletion of aluminum due to the formation of the aluminum-rich bcc structures favors the formation of fcc (A1) in the cell walls of the $x = 1.5$ alloy. This phase, linked with a local VEC of 7.18, shows a similar chemical composition as the secondary phase for $x = 0.8$ (VEC of 7.31) and the secondary phase for $x = 0.2$ (VEC of 7.31). This indicates a change in crystal structure from bcc to fcc for a VEC of ~7.15. Apart from that, the structure of the cell walls of the $x = 0.2$ and 0.8 alloys has been confirmed to be cc (A12), but with local VEC values of 7.23 for $x = 0.2$ and 7.20 for $x = 0.8$.

4. Conclusions

The effect of aluminum content on the microstructure and phase formation of the $Al_xCoCrFeNiTi$ CCA system was studied. All systems show multiphase microstructures with strong variation in chemical composition of the different domains. Four main phases in a mixed solid solution as well as intermetallic phases were identified. By comparing the different alloys, assignments of the structure types were possible. Correlations in phase presence and a preferred nucleation order were found. The specific valence electron concentrations (VECs) of the different domains were determined and discussed in the context of known prediction criteria.

Aluminum stabilizes the high temperature phase, nucleating primarily in the bcc (B2) structure, which is present in the $x = 0.8$ and 1.5 alloys. Chromium- and iron-rich phases with a bcc (A2) structure are present in all samples. For $x = 1.5$, the (B2) and (A2) phases almost entirely fill the microstructure. A small remainder solidifies in the fcc (A1) structure, which appears to be in contrast to the phase prediction for $x = 1.5$ according to both mentioned prediction criteria. An fcc (A1) phase with significantly lower aluminum content compared to (B2) and (A2) phases was present in all samples studied in this work. With decreasing aluminum content, an additional phase with a cc (A12) structure precipitates in $x = 0.2$ and 0.8 alloys. With the further reduction of aluminum in the $x = 0.2$ alloy, the η-$(Ni, Co)_3Ti$ phase precipitates. It can be noted that an increase in aluminum content prevents the precipitation of the A12 centered cluster structure as well as the η-phase.

Author Contributions: Thomas Lindner and Martin Löbel conceived and designed the experiments; Thomas Lindner, Thomas Mehner, and Dagmar Dietrich performed the experiments, analyzed the data, and wrote the paper. Thomas Lampke directed the research and contributed to the discussion and interpretation of the results.

Conflicts of Interest: The authors declare no conflict of interest.

References

1. Cantor, B.; Chang, I.; Knight, P.; Vincent, A. Microstructural development in equiatomic multicomponent alloys. *Mater. Sci. Eng. A* **2004**, *375–377*, 213–218. [CrossRef]
2. Yeh, J.W.; Chen, S.K.; Lin, S.J.; Gan, J.Y.; Chin, T.S.; Shun, T.T.; Tsau, C.H.; Chang, S.Y. Nanostructured High-Entropy Alloys with Multiple Principal Elements: Novel Alloy Design Concepts and Outcomes. *Adv. Eng. Mater.* **2004**, *6*, 299–303. [CrossRef]
3. Miracle, D.; Miller, J.; Senkov, O.; Woodward, C.; Uchic, M.; Tiley, J. Exploration and Development of High Entropy Alloys for Structural Applications. *Entropy* **2014**, *16*, 494–525. [CrossRef]
4. Yeh, J.W. Recent progress in high-entropy alloys. *Eur. J. Control* **2006**, *31*, 633–648. [CrossRef]
5. Tsai, M.; Yeh, J.-W. High-Entropy Alloys: A Critical Review. *Mater. Res. Lett.* **2014**, *3*, 107–123. [CrossRef]
6. Singh, S.; Wanderka, N.; Murty, B.; Glatzel, U.; Banhart, J. Decomposition in multi-component AlCoCrCuFeNi high-entropy alloy. *Acta Mater.* **2011**, *59*, 182–190. [CrossRef]
7. Löbel, M.; Lindner, T.; Kohrt, C.; Lampke, T. Processing of AlCoCrFeNiTi high entropy alloy by atmospheric plasma spraying. *IOP Conf. Ser. Mater. Sci. Eng.* **2017**, *181*, 012015. [CrossRef]
8. Ma, S.; Zhang, Y. Effect of Nb addition on the microstructure and properties of AlCoCrFeNi high-entropy alloy. *Mater. Sci. Eng. A* **2012**, *532*, 480–486. [CrossRef]
9. Zhu, J.M.; Fu, H.M.; Zhang, H.F.; Wang, A.M.; Li, H.; Hu, Z.Q. Synthesis and properties of multiprincipal component $AlCoCrFeNiSi_x$ alloys. *Mater. Sci. Eng. A* **2010**, *527*, 7210–7214. [CrossRef]
10. Zhu, J.M.; Fu, H.M.; Zhang, H.F.; Wang, A.M.; Li, H.; Hu, Z.Q. Microstructures and compressive properties of multicomponent $AlCoCrFeNiMo_x$ alloys. *J. Alloys Compd.* **2010**, *497*, 52–56. [CrossRef]
11. Hsu, C.Y.; Juan, C.C.; Wang, W.R.; Sheu, T.S.; Yeh, J.W.; Chen, S.K. On the superior hot hardness and softening resistance of $AlCoCr_xFeMo_{0.5}$ Ni high-entropy alloys. *Mater. Sci. Eng. A* **2011**, *528*, 3581–3588. [CrossRef]
12. Hume-Rothery, W. Research on the Nature, Properties and Conditions of Formation of Intermetallic Compounds, with Special Reference to Certain Compounds of Tin. *J. Inst. Met.* **1926**, *35*, 295–361.
13. Guo, S.; Ng, C.; Lu, J.; Liu, C. Effect of valence electron concentration on stability of fcc or bcc phase in high entropy alloys. *J. Appl. Phys.* **2011**, *109*, 103505. [CrossRef]
14. Zhu, Z.; Ma, K.; Wang, Q.; Shek, C. Compositional dependence of phase formation and mechanical properties in three CoCrFeNi-(Mn/Al/Cu) high entropy alloys. *Intermetallics* **2016**, *79*, 1–11. [CrossRef]
15. Zhang, K.; Fu, Z. Effects of annealing treatment on phase composition and microstructure of $CoCrFeNiTiAl_x$ high-entropy alloys. *Intermetallics* **2012**, *22*, 24–32. [CrossRef]
16. Yang, X.; Zhang, Y. Prediction of high-entropy stabilized solid-solution in multi-component alloys. *Mater. Chem. Phys.* **2012**, *132*, 233–238. [CrossRef]
17. Wu, P.; Liu, N.; Yang, W.; Zhu, Z.; Lu, Y.; Wang, X. Microstructure and solidification behavior of multicomponent $CoCrCu_xFeMoNi$ high-entropy alloys. *Mater. Sci. Eng. A* **2015**, *642*, 142–149. [CrossRef]
18. Feng, R.; Gao, M.; Lee, C.; Mathes, M.; Zuo, T.; Chen, S.; Hawk, J.; Zhang, Y.; Liaw, P. Design of Light-Weight High-Entropy Alloys. *Entropy* **2016**, *18*, 333. [CrossRef]
19. Soare, V.; Mitrica, D.; Constantin, I.; Badilita, V.; Stoiciu, F.; Popescu, A.-M.; Carcea, I. Influence of remelting on microstructure, hardness and corrosion behaviour of AlCoCrFeNiTi high entropy alloy. *Mater. Sci. Technol.* **2015**, *10*, 1194–2200. [CrossRef]
20. Chuang, M.H.; Tsai, M.H.; Wang, W.R.; Lin, S.J.; Yeh, J.W. Microstructure and wear behavior of $Al_xCo_{1.5}CrFeNi_{1.5}Ti_y$ high-entropy alloys. *Acta Mater.* **2011**, *59*, 6308–6317. [CrossRef]
21. Lee, C.-F.; Shun, T.-T. Age Hardening of the $Al_{0.5}CoCrNiTi_{0.5}$ High-Entropy Alloy. *Metall. Mater. Trans. A* **2014**, *45A*, 191–195. [CrossRef]
22. Gao, M.C.; Yeh, J.W.; Liaw, P.K.; Zhang, Y. *High-Entropy Alloys: Fundamentals and Applications*, 1st ed.; Springer International Publishing: Cham, Switzerland, 2016.